The Journal of Chemical Physics ARTICLE pubs.aip.org/aip/jcp

Effect of molecular permanent dipole moment on guest aggregation and exciton quenching in phosphorescent organic light emitting diodes

Cite as: J. Chem. Phys. 160, 000000 (2024); doi: 10.1063/5.0201560
Submitted: 31 January 2024 • Accepted: 27 May 2024 •
Published Online: 9 99 9999

View Online Export Citation CrossMark

Paul Niyonkuru,[1] Roland Bennett,[1] Michael J. Zachman,[2] and Jeramy D. Zimmerman[1,a)]

AFFILIATIONS

[1] Department of Physics, Colorado School of Mines, Golden, Colorado 80401, USA
[2] Center for Nanophase Materials Sciences, Oak Ridge National Laboratory, Oak Ridge, Tennessee 37831, USA

Note: This paper is part of the JCP Special Topic on Light-matter Interaction at the Nano and Molecular Scale.
[a)] **Author to whom correspondence should be addressed:** jdzimmer@mines.edu

ABSTRACT

This study explores the effect of molecular permanent dipole moment (PDM) on aggregation of guest molecules in phosphorescent host–guest organic light-emitting diodes (OLEDs). Through a combination of photoluminescence measurements, high-angle annular dark-field scanning transmission electron microscopy analysis, and an Ising model based physical vapor-deposition simulation, we show that higher PDM of tris[2-phenylpyridinato-C2,N]iridium(III) guest can actually lead to a reduced aggregation relative to tris[bis[2-(2-pyridinyl-N)phenyl-C](acetylacetonato)iridium(III) when doped into a non-polar host 1,3,5-tris(carbazol-9-yl)benzene. This study further explores the effect of host polarity by using a polar host 3′,5′-di(carbazol-9-yl)-[1,1′-biphenyl]-3,5-dicarbonitrile, and it is shown that the polar host leads to reduced guest aggregation. This study provides a comprehensive understanding of the impact of molecular PDM on OLED material efficiency and stability, providing insights for optimizing phosphorescent OLED materials.

I. INTRODUCTION

Phosphorescent organic light-emitting diode (PhOLED) technology has significantly enhanced the efficiency of organic light-emitting diodes (OLEDs), potentially achieving an internal quantum efficiency close to 100%.[1,2] This improvement is attributed to the incorporation of heavy-metal phosphorescent emitters in a host material. The strong spin–orbit coupling, caused by the heavy atom effect, enables efficient intersystem crossing, allowing both singlet and triple excited states to be emissive.[3–6]

Despite these advancements, the efficiency of PhOLEDs is reduced by quenching processes, such as triplet–triplet annihilation (TTA),[7] triplet-polaron quenching (TPQ), and concentration quenching (CQ).[8,9] We show that CQ is exacerbated by aggregation of guest molecules in the emissive layer (EML) and that aggregation is reduced for a larger permanent dipole moment (PDM) for both guest and host molecules. Molecular aggregation in several physical glassy organics deposited by physical vapor deposition has been shown to be dominated by molecular surface diffusion during film deposition rather than relaxation in the bulk after deposition,[10–12] but this has not been shown for OLED EML materials. During vacuum deposition, evaporated molecules land and diffuse across the surface until they find a metastable configuration and are buried by additional impinging molecules, leading to their kinetic entrapment.[10–14] The aggregation of these molecules in the film is likely influenced by several factors related to this dynamic process, including substrate deposition temperature relative to the glass-transition temperature (i.e., T/T_g)[15–17] and deposition rate.[18–20] For instance, a lower substrate temperature reduces surface diffusion, thereby diminishing aggregation, while a faster deposition rate may prevent the formation of aggregates by rapidly burying molecules and kinetically arresting them.[20] One factor, relevant to this work, that may affect surface diffusion is stronger intermolecular interactions, such as hydrogen bonding, which have been suggested to reduce the rate of surface diffusion in other glassy organic materials.[21–23] This insight into the aggregation mechanism raises questions about the role of material properties, such as polarity, in the aggregation of guest molecules.

This study investigates the influence of molecular permanent dipole moment (PDM) of guest and host materials on the aggregation of guest molecules in thermally vapor-deposited host–guest system EMLs of PhOLEDs. To study the effect of guest PDM, we use a single non-polar host, 1,3,5-tris(carbazol-9-yl)benzene (TCP), and two Ir(III)-based phosphorescent dopants, tris[2-phenylpyridinato-C2,N]iridium(III) [Ir(ppy)$_3$] and tris[bis[2-(2-pyridinyl-N)phenyl-C] (acetylacetonato)iridium(III) [Ir(ppy)$_2$(acac)], which are similar in physical and optical properties but differ significantly in their PDMs of 6.26 and 1.91 D, respectively.[24] To investigate the effect of host polarity, we employ a polar host 3′,5′-Di(carbazol-9-yl)-[1,1′-biphenyl]-3,5-dicarbonitrile (DCzDCN), similar in mass and geometry to the non-polar host TCP, but with a large PDM of 4.1 D.[25,26]

We first investigate the effect of molecular PDM on guest aggregation by analyzing the concentration quenching (CQ) of photoluminescence (PL) efficiency in EML systems of the two guest molecules doped in a non-polar host, TCP. CQ in PhOLEDs is a phenomenon in which the efficiency of light emission decreases as the concentration of the phosphorescent guest material increases. This happens due to interactions between phosphorescent guest molecules, which reduce their ability to emit light.[8,9] As the guest concentration increases, the intermolecular distance of guest molecules becomes smaller and the number of guests with guest-type neighbors increases, which gives rise to the formation of excimer states, which are suggested to act as PL quenching sites for various Ir(III)-based dopants.[27–29] The formation of excimers can also happen at relatively low guest concentrations, if the guest molecules to form clusters in the host matrix. It is noteworthy that this clustering of guest molecules has previously been suggested, but never clearly demonstrated.[7,9,15]

To support the PL analysis, we use high-angle annular dark-field scanning transmission electron microscopy (HAADF-STEM) for direct microscopic measurements of guest aggregation in the EML, extending upon the methodologies used by Reineke *et al.*[7] The heavy iridium core of the dopant molecule allows for scattering contrast with the surrounding organic host, which enables the imaging of guest distribution. Although Reineke *et al.*[7] suggested that clustering is occurring, we note that the two-dimensional (2D) projection in these images can partially obscure the intricate three-dimensional (3D) structure of the material and that typical doping densities will lead to significant numbers of dimers, trimers, and small clusters in fully random host–guest dispersions. To address this limitation and gain a more nuanced understanding of the cluster structure, we implement spatial statistics based point-pattern analysis, which enables statistical verification of these complex three-dimensional structural details. We conclude that CQ dynamics at device-relevant guest concentrations are driven by differing levels of aggregation, which are reduced for larger PDM guest molecules, contrary to what has been previously suggested.[30]

II. EXPERIMENTAL SECTION

Organic materials were used as-purchased from Luminescent Technology Corp. (Lumtec). For all samples, the guest–host EML layers were co-deposited by vacuum thermal evaporation at a rate of ~1 Å/s at a background pressure of 1×10^{-6} Torr and ambient temperature.

Samples for PL measurements were 80 nm-thick and unloaded directly into a nitrogen-atmosphere glovebox and encapsulated with a glass cover using UV-cure epoxy to prevent oxygen intrusion. Temperature-dependent (TD)-PL measurements were performed on samples prepared on Si substrates in an in-house fabricated system consisting of a diode laser (375 nm wavelength, 25 mW power), neutral density filters, a temperature-controlled liquid-nitrogen cooled cryostat, a 450 nm long-pass filter, and an Ocean Optics mini-spectrometer. Initial excitation densities are estimated to be $n_0 < 1.6 \times 10^{23}$ m^{-3} to avoid exciton–exciton quenching effects. The PL results are provided in Fig. S1 of the supplementary material.

Temperature-dependent time-resolved photoluminescence (TRPL) measurements were performed on similar samples in the same cryostat but with an in-house fabricated system designed to collect TRPL spectra from a minimum number of excitation pulses, using a SRS NL100 nitrogen laser (337 nm wavelength, 170 μJ pulse energy), a long-pass filter, a photomultiplier tube (185–900 nm spectral response, gain $> 10^7$, 1.4 ns response time, Thorlabs PMTSS), a preamplifier (DC to 350 MHz, SRS SR445A), and a 100 MHz oscilloscope. Initial excitation densities are estimated to be $n_0 = 1.6 \times 10^{23}$ m^{-3} to minimize TTA processes, as our focus is on excited state lifetimes. The TRPL results are provided in Figs. S2 and S3 of the supplementary material for TCP and DCzDCN systems, respectively.

Photoluminescence quantum yield (PLQY) samples with an EML thickness of 40 nm were similarly prepared on quartz substrates and measured on a Hamamatsu Quantaurus-QY Plus UV-near-infrared (NIR) absolute PL quantum yield spectrometer with an excitation wavelength of 340 nm with a continuous N_2 purge.

HAADF-STEM samples were prepared on single or double layer graphene transmission electron microscopy (TEM) grids (Ted Pella, PELCO). The layer structure is a 10 nm-thick tris(4-carbazoyl-9-ylphenyl)amine (TCTA) base-layer to coat the substrate, a 10 nm-thick EML, and a 10 nm-thick TCTA capping layer; the base and capping layers were designed to prevent dewetting of the EML on the graphene grid during the necessary degassing step. The total thickness of these three layers is kept to a minimum to ensure higher contrast and resolution of the images. Before STEM experiments, the samples were baked at 80 °C for 8 h in vacuum to reduce carbon contamination during imaging. After baking, the samples were rapidly transferred to the instrument vacuum. Aberration-corrected HAADF-STEM imaging was performed on a Nion UltraSTEM 100 instrument operated at 100 keV with a 31 mrad semiconvergence angle. Electron doses of ~ 5×10^4 electrons/Å^2 were utilized for imaging, which minimized Ir atom movement within a given image. Analysis of Ir atom positions was performed using a custom Python code utilizing common packages. Briefly, the process involved removal of low-frequency background image intensity, initial atom position determination, which was performed with single-pixel precision using a difference of Gaussian blob-finding approach, and a refinement of these positions with sub-pixel precision through Gaussian function fitting of each individual atom.[31] The effective depth of field, where the code could identify atom positions, was ~8 nm; however, variations between 5 and 10 nm did not significantly impact the statistical modeling conclusions. Additional details on these measurements and statistical analyses will be provided in an upcoming publication.

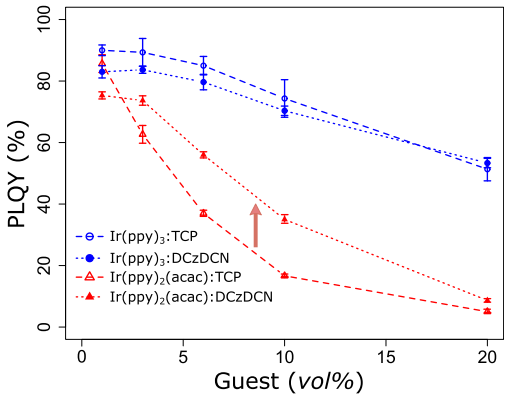

FIG. 1. PLQY dependence on guest vol. % concentration for host–guest systems of $Ir(ppy)_3$(blue circles) and $Ir(ppy)_2(acac)$ (red triangles) doped in either TCP (open symbol with dashed lines) or DCzDCN (closed symbols with dotted lines).

III. RESULTS AND DISCUSSION

A. Effect of guest polarity: Photoluminescence properties

Concentration quenching for various phosphorescent dopants is best quantified through measurements of PLQY vs dopant concentration.[8] In systems with high triplet confinement energy, triplet excitons are predominantly localized on the guest (dopant) molecules.[32] The observed concentration quenching is mainly due to dopant self-quenching, which arises from the formation excimers on guest dimers. This occurs as the average separation between dopant molecules reduces and the number of dopant-type nearest neighbors increases with concentration.[8,9,33,34]

To study the effect of guest PDM on CQ, we conducted our analysis using $Ir(ppy)_3$ and $Ir(ppy)_2(acac)$, separately doped into the non-polar host TCP. This host material was chosen for its large triplet energy (E_T = 2.95 eV[35]), which allows for a sufficiently large confinement energy ($\Delta E_T \approx 0.50$ eV). The findings, depicted in Fig. 1, reveal that both guest systems in the TCP host start with a high

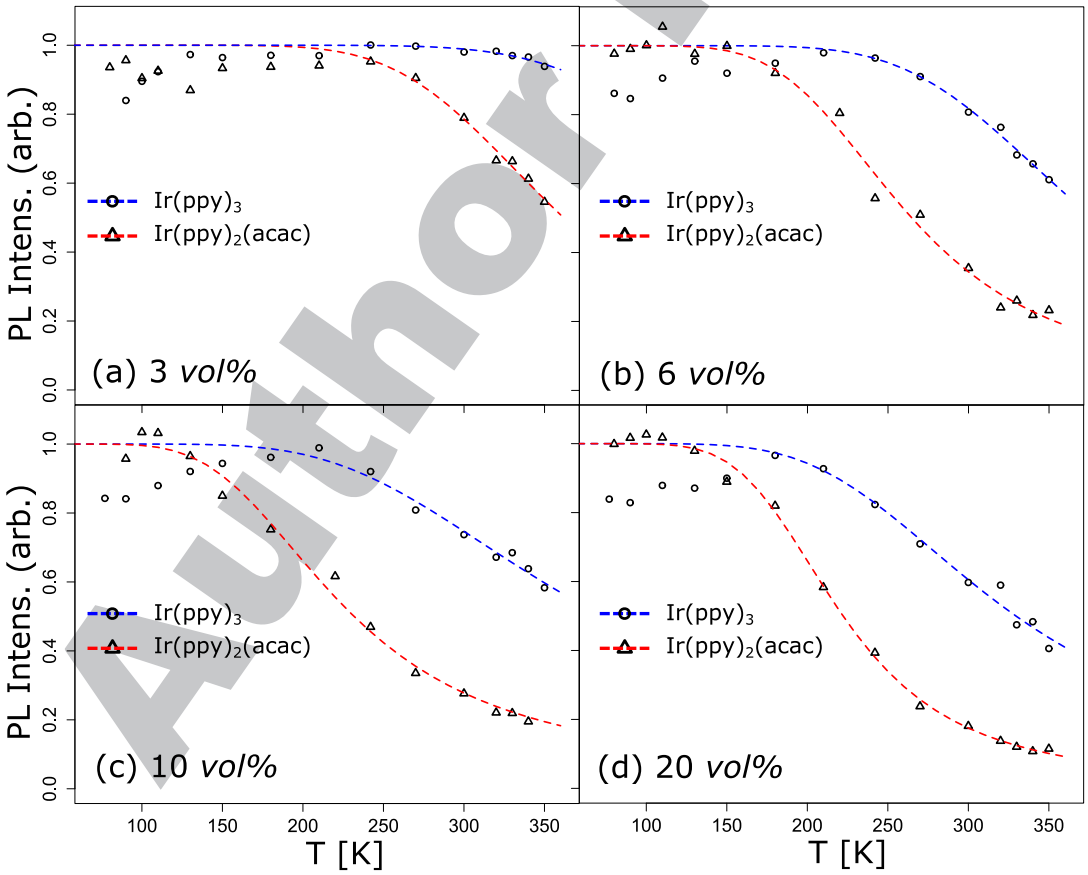

FIG. 2. Normalized TD-PL intensity for $Ir(ppy)_3$ (circles) and $Ir(ppy)_2(acac)$ (triangles), doped in TCP host, fitted to the model in Eq. (7).

PLQY efficiency (about 90%) at a low guest concentration (3 vol. %). However, as the dopant concentration increases, a notable decrease in PL efficiency is observed, characteristic of the self-quenching effect. Notably, the $Ir(ppy)_3$ system maintains a relatively higher PLQY (~60%) at a 20 vol. % concentration, while the PLQY in the $Ir(ppy)_2(acac)$ system significantly decreases, dropping to 5% at the same concentration.

To delve deeper into the PL quenching mechanisms in these systems, we employed temperature-dependent PL analysis. This included studies of PL intensity (Fig. 2) and PL decay rates (Fig. 3). Figure 2 illustrates the temperature-dependent integrated PL intensity for both dopants, represented as $Ir(ppy)_3$ (blue circles) and $Ir(ppy)_2(acac)$ (red triangles), across various doping levels in TCP. For both dopants in a TCP host, we observed a small initial increase in PL intensity with rising temperature, followed by a decrease with further temperature elevation. The specific temperature at which this peak occurs varies between the two dopant systems and is influenced by the doping levels.

This TD-PL behavior has been documented in neat films of $Ir(ppy)_3$ by Kobayashi *et al.*,[36] and a comprehensive explanation was offered using a four-level model, which includes a non-radiative state in addition to the three zero-field splitting (ZFS) sub-states of the lowest emissive triplet metal-to-ligand charge transfer state of the phosphorescent organometallic complexes;[37–39] we herein extend this model for doped films. As later noted by Tsuboi and Aljaroudi,[27] the initial increase in PL, at low temperatures, is attributed to the thermal excitation of triplet excitons from lower ZFS triplet sub-states to the highest, most emissive, triplet sub-state. Further temperature increases lead to exciton transfer from this emissive sub-state to a non-emissive fourth state, causing the observed PL quenching. Tsuboi clarified this PL quenching mechanism in neat $Ir(ppy)_3$ films as a thermally activated transfer of monomer excitation to excimer states, which act as quenching sites[27–29] in a Stern–Volmer formalism.[34]

The dynamics of exciton population in this four-level model are described by the following rate equations and Boltzmann factors:

$$\frac{dN}{dt} = -k_{obs}N = -\sum_{i=1}^{4} k_i n_i, \tag{1}$$

$$n_i = Ne^{\left(-\frac{E_i}{k_B T}\right)}, \tag{2}$$

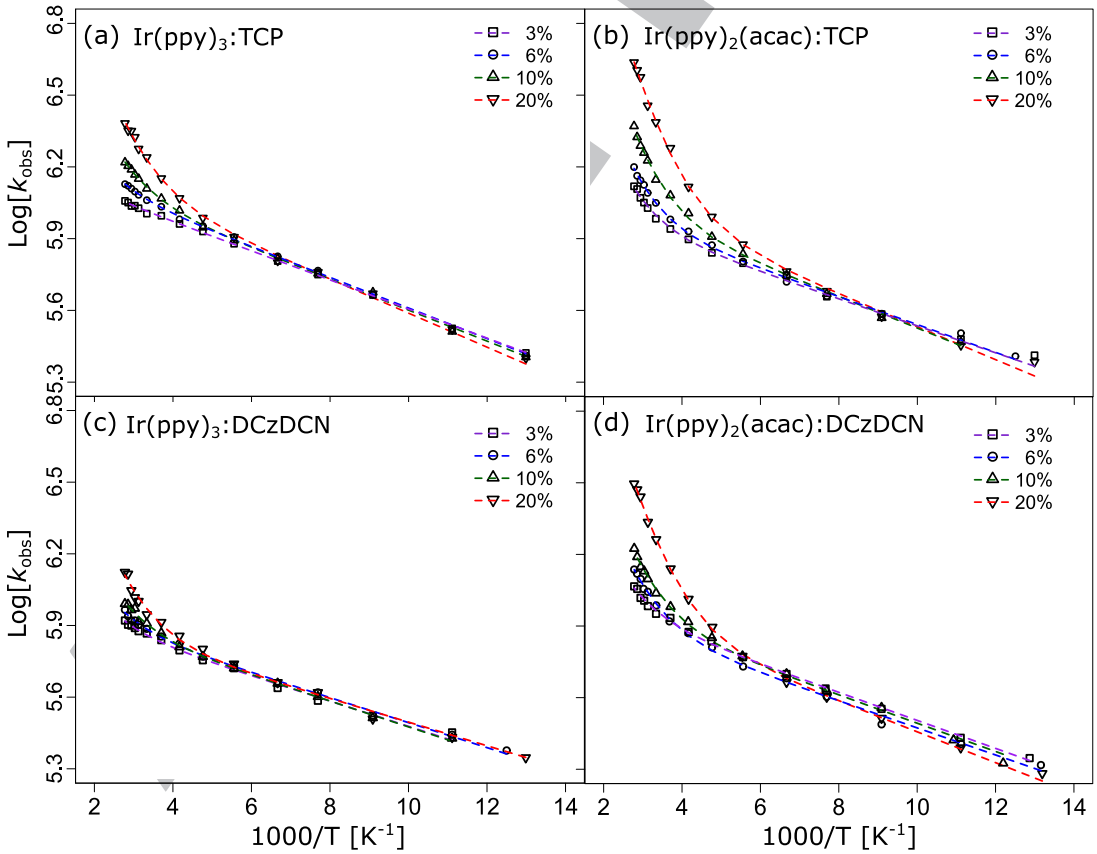

FIG. 3. TD-TRPL emission rate (k_{obs}) data of $Ir(ppy)_3$ at different doping levels in (a) TCP and (c) DCzDCN hosts and $Ir(ppy)_2(acac)$ at different doping levels in (b) TCP and (d) DCzDCN hosts, fitted with the biexponential model in Eq. (5).

where N is the total number of triplet excitons, k_B is the Boltzmann constant, and n_i and k_i represent the population and decay rate of sub-state i, respectively. E_i is the energy difference between the lowest sub-state and sub-state i. By inserting Eq. (2) into Eq. (1), the average observed decay rate of excitons, k_{obs}, and the relative phosphorescence efficiency ϕ_p can be calculated as

$$k_{obs} = k_1 + k_2 e^{\left(\frac{-E_2}{k_B T}\right)} + k_3 e^{\left(\frac{-E_3}{k_B T}\right)} + k_4 e^{\left(\frac{-E_4}{k_B T}\right)}, \quad (3)$$

$$\phi_p = \frac{k_1 + k_2 e^{\left(\frac{-E_2}{k_B T}\right)} + k_3 e^{\left(\frac{-E_3}{k_B T}\right)}}{k_1 + k_2 e^{\left(\frac{-E_2}{k_B T}\right)} + k_3 e^{\left(\frac{-E_3}{k_B T}\right)} + k_4 e^{\left(\frac{-E_4}{k_B T}\right)}}. \quad (4)$$

At temperatures above 100 K, k_1 and k_2 terms are orders of magnitude lower than k_3,[36,37] allowing Eqs. (3) and (4) to be simplified to

$$k_{obs} = k_3 e^{(-E_3/k_B T)} + \alpha k_4 e^{(-E_4/k_B T)}, \quad (5)$$

$$\phi_p = \frac{k_3 e^{(-E_3/k_B T)}}{k_3 e^{(-E_3/k_B T)} + \alpha k_4 e^{(-E_4/k_B T)}}. \quad (6)$$

We extend the previous models for neat films to work with doped films by including α, a dimensionless parameter related to the concentration of quenching states within the system. At low dopant concentrations, α is nearly zero, leading to a conventional three-level monomer-like system. As the dopant concentration increases, α rises due to an increased presence of quenching states (i.e., excimer states),[33,34] which would result from an increased amount of dopant aggregation (e.g., dimers). The significance of α is explored by fitting temperature-dependent exciton decay rates (k_{obs}) in Fig. 3, obtained from TRPL measurements (provided in Figs. S1 and S2 of the supplementary material), with the biexponential model in Eq. (5). The fit results are presented in Figs. 4 and 5.

In Fig. 4(a), the values of E_3 (~12 meV) align well with the reported activation energy between the second and third monomer

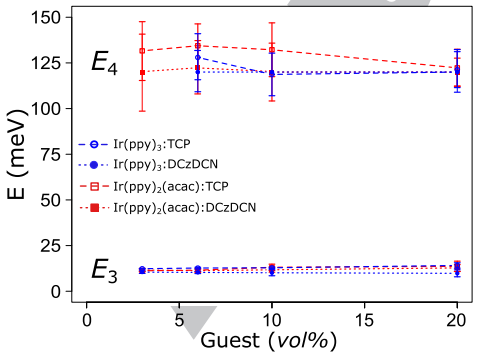

FIG. 4. Comparative analysis of extracted fit parameters from TD-TRPL emission rate data in Fig. 3 (TCP and DCzDCN hosts). E_3 and E_4 for host–guest systems of Ir(ppy)$_3$ (blue circles) and Ir(ppy)$_2$(acac) (red squares) doped in either TCP (open symbols and dashed lines) or DCzDCN (closed symbols and dotted lines).

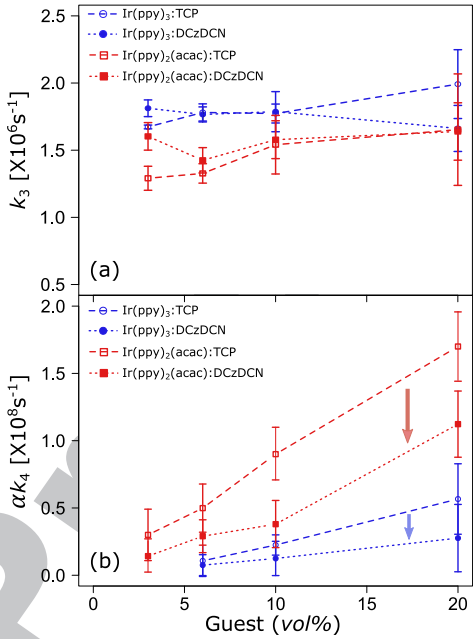

FIG. 5. Extracted fit parameters from TD-TRPL emission rate data in Fig. 3 (TCP and DCzDCN hosts). (a) k_3 and (b) αk_4 for host–guest systems of Ir(ppy)$_3$ (blue circles) and Ir(ppy)$_2$(acac) (red squares) doped in either TCP (open symbols and dashed lines) or DCzDCN (closed symbols and dotted lines).

triplet sub-states,[40] while the obtained E_4 (~120 meV) is consistent with the activation energy for excimer formation.[27] Figure 5(a) shows that the radiative decay rate k_3 remains constant across the studied range of emitter concentrations, while the quenching rate, corresponding to the product αk_4 in Fig. 5(b), increases with increasing doping concentration. Similar behaviors have been observed by Kawamura *et al.*, who attributes the quenching process to a Förster energy transfer.[9] The quenching rate rises to about 5×10^7 s^{-1} at a guest doping concentration of 20 vol. % for Ir(ppy)$_3$, while it is approximately three times larger for Ir(ppy)$_2$(acac). Assuming that the decay rate k_4 is similar for Ir(ppy)$_3$ and Ir(ppy)$_2$(acac), this increase in α would be indicative of more aggregation in Ir(ppy)$_2$(acac) relative to Ir(ppy)$_3$.

In Fig. 2, we show that, at each concentration studied, the PL quenching in Ir(ppy)$_2$(acac) systems is more pronounced than in the corresponding Ir(ppy)$_3$ systems. For further analysis, we consider that $\phi_p(T) = I(T)/I_0$. Here, I_0 is the maximum PL intensity, occurring when the temperature is low enough that there is no transfer of excitation to the quenching state. We express the TD-PL intensity $[I(T)]$ in a form similar to the classic Stern–Volmer equation,[34]

$$I(T) = \frac{I_0}{1 + Ae^{(-E_a/k_B T)}}, \quad (7)$$

where $A = \alpha(k_4/k_3)$ and the activation energy $E_a = E_4 - E_3$.

Applying this model at temperatures above 200 K—where the effects of thermal transfer between the triplet sub-states are efficient

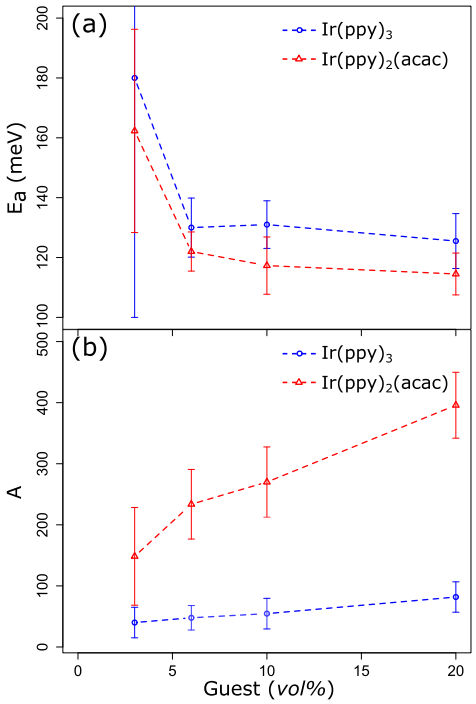

FIG. 6. Fit parameters to TD-PL data in Fig. 2 data with Eq. (7) for $Ir(ppy)_3$ (blue circles) and $Ir(ppy)_2(acac)$ (red triangles) doped in TCP host.

and emission from the third sub-state dominates—we extract key insights into the quenching process. These are depicted in Fig. 6, illustrating (a) the activation energy E_a, transitioning from the third triplet sub-state to the fourth quenching state, and (b) the prefactor A, which is proportional to the concentration of quenching states. In agreement with previous TD-TRPL analysis, the activation energy is roughly 120 meV for both dopants. The quenching prefactor A increases with guest concentration; however, the growth in A is more rapid for $Ir(ppy)_2(acac)$ compared to $Ir(ppy)_3$.

In summary, PL quenching increases with increased doping concentration. This increase is notably more substantial in the $Ir(ppy)_2(acac)$ systems than in $Ir(ppy)_3$. We attribute this to a higher degree of aggregation in the $Ir(ppy)_2(acac)$ systems, a conclusion bolstered by direct microscopic analysis (see below), employing HAADF-STEM measurements and spatial-statistics based point-pattern analysis (PPA) on thin films of the two host–guest systems.

B. Effect of guest polarity: HAADF-STEM analysis

HAADF-STEM provides a 2D projection of the spatial distribution of guest molecules within the depth of field of the instrument, thanks to the high scattering contrast from the heavy iridium core of the dopant molecules. In Fig. 7, we present the HAADF-STEM experimental results on thin films of host–guest systems containing 10 vol. % of $Ir(ppy)_3$ doped in TCP host (example micrograph shown in Fig. 7(a) with the extracted molecular positions in Fig. 7(b)). Additional HAADF-STEM images and corresponding

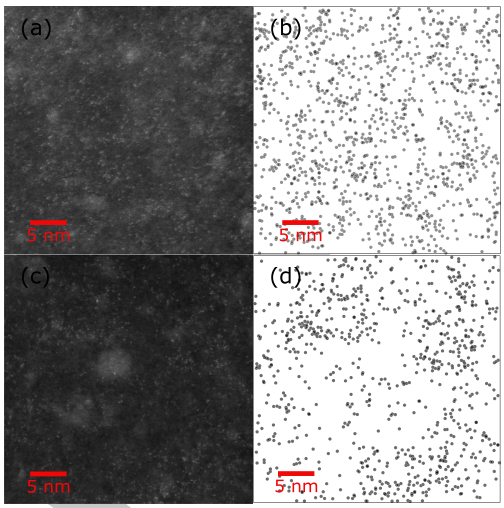

FIG. 7. (a) HAADF-STEM images and (b) extracted coordinates for 10 vol. % $Ir(ppy)_3$, (c) HAADF-STEM images and (d) extracted coordinates for $Ir(ppy)_2(acac)$, all in a TCP host.

PPA are provided in the supplementary material (Figs. S4 and S5). Similar results are displayed for the $Ir(ppy)_2(acac)$ system doped in TCP host, in images (c) and (d). A visual inspection of Figs. 7(a) and 7(b) suggests that the $Ir(ppy)_3$ molecules are relatively evenly dispersed across the field, while there is a long-range density variation for $Ir(ppy)_2(acac)$ in Figs. 7(c) and 7(d).

Analysis of the guest locations is performed by applying Ripley's K- (Fig. 8) and G-function (Fig. 9) based spatial-statistics[41–44] to the experimentally observed point patterns. For $Ir(ppy)_3$ and $Ir(ppy)_2(acac)$ doped in the non-polar host TCP, K-function analyses are presented in Figs. 8(a) and 8(b), respectively (additional analyses are provided in Figs. S5–S7 of the supplementary material). Ripley's K-function is a measure of the number of like-points within each evaluation radius r (Ir-cores, in this case). To understand these data, we simulate 3D patterns of guest molecules on a simulated random close-packed (RCP) lattice of appropriate thickness, collapse the data into 2D, and perform the same point-pattern analysis. We subtract the mean of 100 simulations of random dispersions of guest identities on the RCP lattice to create $\tilde{K}_g(r)$. We plot the 95% acceptance intervals in Fig. 8 for the random simulation (tan band); randomly dispersed data are expected to fall within this band 95% of the time. When the experimental data are positive and above the acceptance interval band, this suggests that there is a significant degree of clustering occurring at that analysis radius.

The G-function is the cumulative distribution of the distance from each guest Ir-core to the nearest guest core, providing complementary details on short-range clustering (e.g., providing a strong signal for guest dimers). $\tilde{G}_g(r)$ (shown in Fig. 9) is similarly calculated from $G_g(r)$ by subtracting the median of the random relabeling simulations at each r, and a deviation above the envelopes indicates that the molecules are more closely spaced than would be expected for a spatially random dispersion.

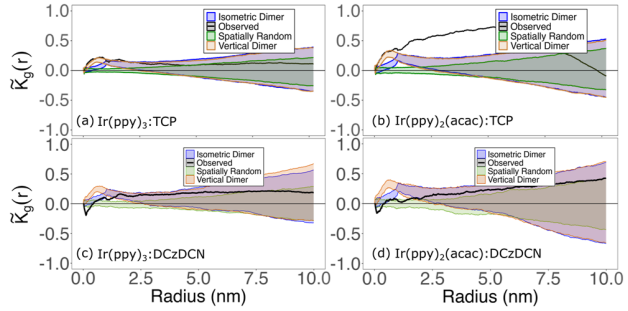

FIG. 8. Ripley's K-function analysis of 10 vol. % guest doping for (a) $Ir(ppy)_3$ in TCP, (b) $Ir(ppy)_2(acac)$ in TCP, (c) $Ir(ppy)_3$ in DCzDCN, and (d) $Ir(ppy)_2(acac)$ in DCzDCN.

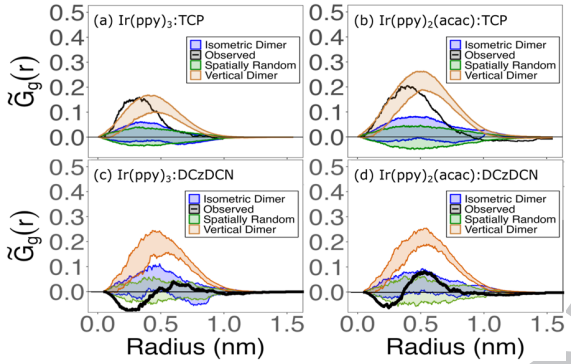

FIG. 9. Ripley's G-function analysis of 10 vol. % guest doping for (a) $Ir(ppy)_3$ in TCP, (b) $Ir(ppy)_2(acac)$ in TCP, (c) $Ir(ppy)_3$ in DCzDCN, and (d) $Ir(ppy)_2(acac)$ in DCzDCN.

Acceptance interval envelopes for $\tilde{K}_g(r)$ and $\tilde{G}_g(r)$ for simulated point patterns of randomly oriented dimers and preferentially vertically oriented dimers are also provided in Figs. 8 and 9, respectively, to provide additional possible point patterns of the samples. For $\tilde{K}_g(r)$ analysis of $Ir(ppy)_3$ in Fig. 8(a), the experimental data fall within the acceptance band for the vertical dimer model across the entire radius range. Additional sensitivity to the short-range ordering for $\tilde{G}_g(r)$ analysis of $Ir(ppy)_3$ in Fig. 9(a) suggests that the typical spacing for nearest neighbors is even closer than would be expected for the vertical dimers that are modeled by our RCP lattice. The molecular shapes and molecular dynamics of stacking is not accounted for in these statistical models, but given the qualitative agreement to the models and that many dimers and short chains are visually present in the data, no additional simulations are provided here. Additional details on this analysis will be provided in a separate publication.[45]

The $\tilde{K}_g(r)$ analysis of $Ir(ppy)_2(acac)$ in Fig. 8(b) is slightly more complicated. The increase at radius values below 1 nm is again consistent with vertical dimers, but the peak at roughly 2.5–5 nm is indicative of long-range clustering behavior with domains of roughly twice the radius value of the peak,[43,46] in qualitative agreement with the data shown in Fig. 9(b). The $\tilde{G}_g(r)$ analysis in Fig. 9(b) supports that many of the guests exist in vertical dimer configurations. In aggregate, these data suggest that $Ir(ppy)_2(acac)$, with its significantly lower PDM, can diffuse over many nanometers before finding a local minimum and being buried by additional impinging molecules, while $Ir(ppy)_3$ has a shorter surface diffusion length. Again, additional details on this analysis will be provided in a separate publication.[45]

This finding of more aggregation in $Ir(ppy)_2(acac)$ compared to $Ir(ppy)_3$ in a TCP host is in agreement with the relevant PL measurements of Figs. 1–5, which would be consistent with higher aggregation-based quenching values for $Ir(ppy)_2(acac)$. In addition, these microscopic analyses uncover a tendency for both dopant systems to form vertically oriented dimers or stacks. The reasons behind the observed behavior are further explored through the analysis of simulated model morphologies in Sec. IV.

C. Effect of a polar host: Photoluminescence properties

To investigate the effect of host polarity, we employed a polar host DCzDCN, with a PDM of 4.1 D,[25,26] but similar in mass and geometry to the non-polar host TCP. The overall PLQY in Fig. 1 starts lower for both guests in DCzDCN relative to TCP hosts, presumably due to the lower triplet confinement energy, but the rate at which it decreases with concentration is less, particularly in the case of $Ir(ppy)_2(acac)$. Similar to the non-polar host (TCP) systems [Figs. 3(a) and 3(b)], the dependence of exciton decay rate k_{obs} on temperature for $Ir(ppy)_3$ and $Ir(ppy)_2(acac)$ in the polar host (DCzDCN), shown in Figs. 3(c) and 3(d), exhibits two distinct exponential regions. The initial increase in k_{obs} with temperature, similarly attributed to the thermal excitation of triplet excitons to the highest, most emissive triplet sub-state, has a similar activation energy, $E_3 \approx 12$ meV (Fig. 4), in the polar host (DCzDCN) systems as in the non-polar host (TCP) systems. A further temperature increase leads to exciton transfer to the non-emissive fourth state associated with excimer formation on aggregates.[27,34] This thermally activated process also exhibits a similar activation energy ($E_4 \approx 120$ meV) in DCzDCN systems as in TCP systems. Similar to the non-polar host (TCP) systems, this second region gets more pronounced with increasing guest concentration because of increased aggregate formation. A close look at the TD k_{obs} data in Fig. 3, however, shows that this second activation to the non-emissive state is less pronounced in DCzDCN systems [Figs. 3(c) and 3(d)] relative to corresponding TCP systems [Figs. 3(a) and 3(b)]. This observation is further explored in Fig. 5.

As discussed in Sec. III A, Fig. 5 shows the extracted exciton decay rates k_3 and αk_4 from the TD k_{obs} data in Fig. 3 using the model in Eq. (5). The radiative decay rates k_3, associated with guest monomer emission, remain nominally constant across the studied range of emitter concentrations in the two host systems, indicating that monomers of the two guest emitters [i.e., $Ir(ppy)_3$ and $Ir(ppy)_2(acac)$] have a similar emissive rate and changing host PDM does not affect monomer emissive properties. Meanwhile, as discussed for TCP systems, the PL quenching rate, corresponding to the product αk_4, increases with increasing doping concentration and rises much faster for $Ir(ppy)_2(acac)$ relative to $Ir(ppy)_3$ systems, which was attributed to more aggregation in $Ir(ppy)_2(acac)$ relative to $Ir(ppy)_3$. Now looking at both guest dopants in the polar host

material DCzDCN (closed symbols and dotted lines), we observe an overall shift to lower magnitudes for αk_4, relative to the non-polar host systems (open symbols and dashed lines). This suggests that there is reduced aggregation for both guest molecules when doped in the polar host DCzDCN as compared to the non-polar TCP.

In summary, PL quenching is reduced for both studied guest dopants, $Ir(ppy)_3$ and $Ir(ppy)_2(acac)$, when doped in the polar host DCzDCN compared to when doped in the non-polar host TCP. We attribute this to a reduced degree of guest aggregation in the polar DCzDCN systems, a conclusion supported by direct microscopic analysis, employing HAADF-STEM measurements and spatial-statistics based point pattern analysis (PPA) on thin films of the two guests doped in both host systems in Figs. 8 and 9 and discussed below.

D. Effect of a polar host: HAADF-STEM analysis

In Fig. 10, we present the HAADF-STEM experimental results and extract guest locations for 10 vol. % $Ir(ppy)_3$ [(a) and (b)] and $Ir(ppy)_2(acac)$ [(c) and (d)] doped in the polar host DCzDCN. A comparative analysis of the spatial distributions of the two guests in the non-polar and polar hosts using the Ripley's K-function, in Fig. 8, shows that the polar host DCzDCN [(c) and (d)] significantly reduces the aggregation of both $Ir(ppy)_2(acac)$ and $Ir(ppy)_3$, relative to when doped into TCP [(a) and (b)]. The K-function analysis reveals a nuanced view of how spatial relationships evolve across different scales. At shorter distances ($r < 1$ nm), the function's deviation below the envelope of a random distribution for both $Ir(ppy)_2(acac)$ and $Ir(ppy)_3$ in DCzDCN suggests pronounced guest inhibition, likely due to the polar DCzDCN host strongly interacting with the guest molecules. This inhibition is in contrast to the observed aggregation for both guests in the non-polar host TCP, where both $Ir(ppy)_3$ and $Ir(ppy)_2(acac)$ guest molecules tend to fall within the vertical dimer envelopes. More HAADF-STEM and spatial point-pattern analyses for DCzDCN systems are provided in Figs. S6 and S7 of the supplementary material.

Furthermore, the transition to larger radii ($r > 1$ nm) in the K-function underscores a critical shift toward less deviation from the random point distribution of the polar host DCzDCN compared to TCP, particularly for $Ir(ppy)_2(acac)$. This observation suggests that the polar host environment disrupts the propensity for large-scale aggregation, promoting a more well-dispersed dopant distribution. Such a distribution is crucial for minimizing guest–guest interactions, which, as established, play a pivotal role in concentration quenching phenomena. The decreased aggregation and enhanced dispersion in the polar host directly correlate with the improved PLQY, as seen in Fig. 1, and performance metrics observed in TD-TRPL analyses of Fig. 5, confirming the beneficial impact of host material polarity on PhOLED efficiency.

Through a detailed examination of these spatial patterns, this analysis not only complements the photophysical insights from PLQY and TD-TRPL studies but also enriches our understanding of the fundamental mechanisms governing dopant distribution and interaction within PhOLED systems. The ability of the polar host DCzDCN to mitigate aggregation and promote guest inhibition at short distances emerges as a key factor in optimizing PhOLED design and performance.

IV. MORPHOLOGY SIMULATION

A. Ising model for aggregation

Here, we employ analysis of model morphologies simulated based on the kinetic Monte Carlo (KMC) and Ising clustering model, explain the observed results, and elucidate on how a larger dopant molecule permanent-dipole moment leads to the formation of small aggregates and the observed vertical stacking. The foundational framework for developing model morphologies for small molecule blends was initially introduced by Peumans *et al.*[47] drawing inspiration from the Kawasaki spin-exchange Ising model.[48] Subsequently, Watkins *et al.*[49] simplified and adapted this concept to KMC simulations.

In our methodology, molecules are conceptualized as structureless points on a cubic grid, with predefined interaction energies. While acknowledging its limitations, this approach enables simulations of device-scale systems that are still unfeasible with techniques such as molecular dynamics.

The Ising clustering model entails generating a three-dimensional cubic lattice, with host or guest sites randomly assigned based on a specified host–guest ratio. Periodic boundary conditions are imposed in the x and y directions, while hard boundaries are enforced in the z-direction to mimic a thin film. The standard Ising Hamiltonian is employed to compute the energy of site i,

$$\epsilon_i = -\frac{J_{\mathrm{Host,Guest}}}{2(d_{ij}/a)} \sum_j \left(\delta_{t_i,t_j} - 1\right). \tag{8}$$

Here, a represents the lattice constant, δ_{t_i,t_j} is the Kronecker delta, and t_i and t_j signify the types of molecules occupying sites i and j, respectively, with a separation of distance d_{ij}. The parameter $J_{\mathrm{Host,Guest}}$ denotes the interaction energy, reflecting the difference

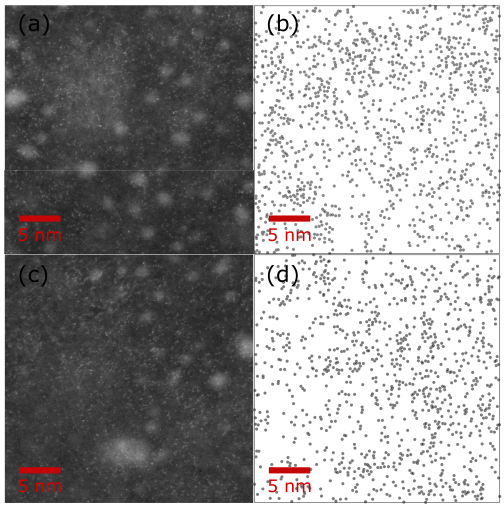

FIG. 10. (a) HAADF-STEM images and (b) extracted coordinates for 10 vol. % $Ir(ppy)_3$, (c) HAADF-STEM images and (d) extracted coordinates for $Ir(ppy)_2(acac)$, all in a DCzDCN host.

between host–host (J_{H-H}) or guest–guest interaction energy (J_{G-G}) and host–guest interaction energy (J_{H-G}),

$$J_{Host} = J_{H-H} - J_{H-G}, \tag{9}$$

$$J_{Guest} = J_{G-G} - J_{H-G}. \tag{10}$$

Following lattice generation, the aggregation process is simulated by allowing the system's energy to relax over a series of iterations, i.e., Monte Carlo steps (MCS). The aggregation process involves swapping nearest-neighbor sites, where two adjacent sites with different types are randomly selected from the lattice. The total energy change of the system resulting from swapping the sites, denoted $\Delta\epsilon$, is computed and utilized to calculate the probability of the swapping event,

$$P(\Delta\epsilon) = \frac{e^{-\Delta\epsilon/(k_B T)}}{1 + e^{-\Delta\epsilon/(k_B T)}}. \tag{11}$$

To simulate aggregation in organic light-emitting diodes (OLEDs), we employed an open-source simulation tool named Ising-OPV, developed by Heiber and Dhinojwala.[50] Originally designed for generating bulk-heterojunction (BHJ) morphologies in organic photovoltaics, we tailored the code to produce model morphologies for surface diffusion dominated physical vapor-deposition (PVD).

B. Physical vapor-deposition algorithm

In systems made by PVD, similar to OLED films, molecular aggregation is primarily governed by rapid surface diffusion, rather than relaxation within the bulk of the material.[10–12] To simulate these PVD systems more accurately, we have made specific alterations to the BHJ algorithm, which typically emphasizes bulk relaxation in aggregation.

The BHJ algorithm models molecular aggregation by randomly selecting and swapping two adjacent sites within a 3D lattice to reduce the system's energy. However, in our modified PVD algorithm, only the molecules in the surface layer are allowed to swap positions, while those in the lower layers are fixed. This process is repeated for a certain number of iterations, given by the number of MCS before locking the surface and adding a new layer of molecules and repeating. This layer-by-layer approach, starting from the bottom layer and moving upward, replicates the restricted diffusion of molecules in the bulk of thin films while letting the surface relax. Example model morphologies created using the PVD algorithm are illustrated in Fig. 11, with further analysis in Fig. 12.

Figure 12(a) shows how the size of molecular clusters, resulting from guest molecule aggregation, varies with the interaction energy between guest molecules (J_{Guest}) and the number of MCS. The number of MCS is related to the time allowed for surface molecules to diffuse before being fixed in a metastable state by newly deposited molecules. Experimentally, this time is inversely proportional to the

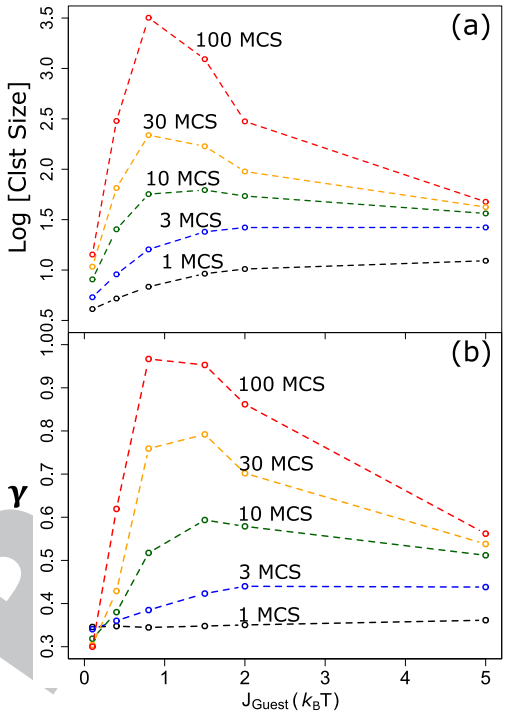

FIG. 12. Morphology analysis for a 10% guest–host ratio system with a fixed $J_{Host} = 0.4k_BT$. (a) Cluster size and (b) verticality of cluster measured by parameter γ.

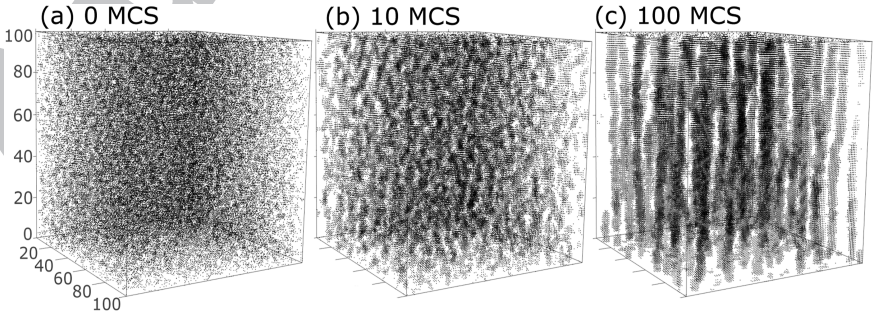

FIG. 11. Model morphologies of a binary host–guest system produced with the PVD model with $J_{Host} = 0.4k_BT$ and $J_{Guest} = 1.5k_BT$ at different MCS.

deposition rate. Several studies of PVD organic semiconductors have indicated that a lower deposition rate allows for further equilibration at the surface toward preferred structures.[13,20,51,52] Our simulations similarly show that the cluster size increases with a higher number of MCS. In our experiments, deposition rates were kept at 1 Å s^{-1}. Assuming the effective diameter of each molecule being 1 nm means that each molecule has 10 s to diffuse before being covered by incoming molecules. While we do not know the exact number of MCS steps this correlates with, the deposition rate is many orders of magnitude greater than molecular vibrations, suggesting that we should be considering larger values of MCS.

For MCS values greater than 10, the relationship between the cluster size and J_{Guest} displays a non-monotonic pattern. Initially, the cluster size increases with J_{Guest} until a critical threshold ($J_{Guest} \approx 1k_BT$), beyond which, further increases in J_{Guest} reduce the cluster size. The PDM of $Ir(ppy)_3$ and $Ir(ppy)_2(acac)$, at 6.26 and 1.81 D respectively, correspond to dipole–dipole (i.e., Keesom) interaction energies of roughly 204 and 47 meV,[24] which are added to the other existing intermolecular forces. These energies are $\sim 8.1k_BT$ and $1.9k_BT$ at room temperature. $Ir(ppy)_2(acac)$, with its lower dipole–dipole interaction energy, is just to the right of the peak of the curves in Fig. 12, while $Ir(ppy)_3$ is well off of the right side of the graph, suggesting a mechanism for why $Ir(ppy)_2(acac)$ forms larger aggregates than $Ir(ppy)_3$.

This phenomenon is a function of the complex interplay between van der Waals intermolecular interactions and molecular surface diffusion. An increase in intermolecular interaction energy (e.g., due to the addition of permanent dipole–permanent dipole based Keesom forces) enhances the attraction between guest molecules, thereby promoting the formation of guest aggregates. However, a larger dipole moment leads to stronger intermolecular interactions, both Keesom-like interactions between two guest molecules and Debye-like interactions between the guest and non-polar host molecules. Such interactions between surface molecules and the fixed bulk create a higher kinetic diffusion barrier, which slows surface diffusion. This is in qualitative agreement with our PL and HAADF-STEM data and previous experimental studies in organic molecular glasses, which suggest that strong intermolecular interactions slow down surface diffusion.[53,54]

Another interesting aspect of these morphologies is the formation of vertical clusters, as observed in the examples presented in Figs. 11(b) and 11(c). We assess cluster verticality through a parameter γ defined as

$$\gamma = \frac{S_z^2}{S_x^2 + S_y^2 + S_z^2}. \tag{12}$$

Here, S_x^2, S_y^2, and S_z^2 represent the standard deviation in the positions of sites in the x, y, and z directions within a cluster, respectively. For an isotropic cluster, where all three directions are equally distributed, γ equals 1/3. In the case of a cluster with a preferred horizontal orientation, where S_x^2 and S_y^2 are large while S_z^2 is small, γ is less than 1/3. Finally, for clusters with a vertical orientation, where S_z^2 is larger than S_x^2 and S_y^2, γ is greater than 1/3.

The results in Fig. 12(b) demonstrate that clusters produced by the PVD algorithm exhibit a vertical orientation and are qualitatively consistent with our experimental findings of vertical clusters obtained through HAADF-STEM methods. Similar to cluster size trends, cluster verticality also increases with the number of MCS and reaches a critical point $J_{Guest} \approx 1k_BT$, beyond which an increase in J_{Guest} leads to reduced verticality.

The tendency for vertical stacking in these clusters is attributed to the dominant role of surface diffusion in aggregation, while bulk relaxation is restricted. Essentially, incoming guest molecules in the surface layer undergo diffusion due to thermal energy, moving across the surface until they find low-energy states. This occurs when they bind to polar molecules located in the bulk of the film. Such a binding process preferentially leads to vertical stacking of the guest molecules as observed in these simulations and HAADF-STEM results. In summary, we conclude that the clustering of polar guest molecules in a non-polar host is not thermodynamically controlled, but kinetically limited.

In PVD systems, aggregation is primarily driven by the surface diffusion of impinging molecules,[10–12] with the surface diffusivity that exhibits an Arrhenius behavior,

$$D_S = D_0 e^{-E_{diff}/k_BT}, \tag{13}$$

where D_0 is a diffusion coefficient and E_{diff} is the kinetic barrier to surface diffusion. E_{diff} is proportional to the adsorbed atom's binding energy.

The reduced guest aggregation in DCzDCN systems can be understood to originate from the high-polarity host material fostering stronger Keesom and Debye electrostatic binding interactions with adsorbed polar molecules, elevating their kinetic barrier for surface diffusion (E_{diff}). This hampers the diffusivity of adsorbed molecules on the surface (D_S), leading to a reduction in aggregation. They are dependent on the host's permanent dipole moment as shown in the following equations:

$$U_{dd} = -2\mu_1\mu_2/r^3, \tag{14}$$

$$U_{di} = -4\alpha_2\mu_1^2/r^6. \tag{15}$$

These interactions, by altering the energy landscape that the molecules on the surface experience, directly influence the rate and extent of aggregation through modified surface diffusion dynamics.

While reduced surface diffusion accounts for diminished aggregation, the observed effect of inhibition at small distances is specifically analyzed through simulations. Ising KMC simulations with a PVD algorithm provide insights into this inhibition effect. In the Ising model, the interaction energies driving phase segregation—J_{Host} and J_{Guest}—are calculated by subtracting the host–guest interaction energy (J_{H-G}) from the host–host (J_{H-H}) and guest–guest (J_{G-G}) interaction energies, as shown in Eqs. (9) and (10), respectively.

To conduct our simulations, we model scenarios where the guest molecule remains constant, maintaining a steady J_{G-G}, while varying the host to increase both J_{H-H} and J_{H-G}, but keeping their difference, J_{Host}, constant at $0.6k_BT$. This setup leads to a constant J_{Host} with varying J_{Guest} interaction energies. In Fig. 13, the K- and G-function analyses of guest distribution in model morphologies, containing 10% guest concentration and simulated over 30 MCS, demonstrate the conditions under which guest molecule inhibition occurs. Specifically, inhibition begins when J_{H-G} not only exceeds J_{G-G} but also when the condition $(J_{H-G} - J_{G-G}) > (J_{H-H} - J_{H-G})$

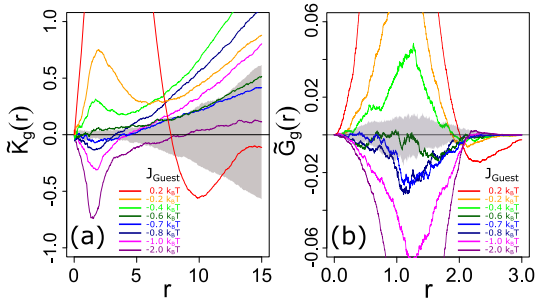

FIG. 13. Ripley's (a) K- and (b) G-function analyses of simulated model morphologies of 10% guest doping with a fixed $J_{Host} = 0.6k_BT$ and varying J_{Guest}.

is satisfied. Such a condition implies a preference for host molecules to bind to guest molecules over the latter aggregating among themselves, due to the larger J_{H-G} compared to J_{G-G}. This dynamic effectively inhibits close-range aggregation of guest molecules.

The K-function analyses validate the inhibition effect by illustrating how, under circumstances where J_{H-G} is significantly greater than J_{G-G} ($J_{Guest} < 0$), there is a pronounced preference for host molecules to associate with guest molecules. This preference inhibits the aggregation of guest molecules when they are in close proximity, confirming the detailed dynamics behind the observed inhibition at small distances within the simulated vapor-deposited systems.

In real system, these interaction energies (J_{G-G}, J_{H-H}, J_{H-G}) are of van der Waals nature, Keesom and Debye, as defined in Eqs. (14) and (15). Depending on host and guest molecular shape and size, the separation r between dipoles will play a crucial role in determining the relative magnitude of interaction energies between different species; hence, it is possible to have host–guest interactions being larger than guest–guest interaction energies, particularly when the geometry of these two molecules is considered.

V. CONCLUSION

In conclusion, this study presents insights into how the PDM of guest and host molecules impacts the aggregation behavior and PL properties of PhOLEDs. By analyzing two Ir(III)-based phosphorescent dopants, $Ir(ppy)_3$ and $Ir(ppy)_2(acac)$, in non-polar (TCP) and polar (DCzDCN) hosts, several key findings were observed.

Guest molecules with a higher PDM, such as $Ir(ppy)_3$, exhibited less aggregation and lower concentration quenching compared to those with a lower PDM, such as $Ir(ppy)_2(acac)$. This reduced aggregation leads to higher PLQY and better efficiency in PhOLED emissive layers. Simulations revealed that a larger PDM increases intermolecular interactions, which inhibit surface diffusion and consequently reduce aggregation.

Both guest molecules tested show significantly reduced aggregation when doped into the polar host (DCzDCN) compared to the non-polar host (TCP). This reduction in aggregation was observed through both PL and HAADF-STEM analyses. The polar host material (DCzDCN) led to lower quenching rates and higher PLQY for both guest molecules. The additional intermolecular interactions between the polar host and guest molecules create a higher kinetic barrier for surface diffusion, which reduces guest aggregation and improves the overall performance of the PhOLEDs.

The KMC simulations using the Ising model and a modified PVD algorithm supported the experimental data. These simulations demonstrated that higher PDMs in both guest and host molecules lead to smaller and more vertically oriented aggregates. The polar host environment disrupts large-scale aggregation by promoting a well-dispersed dopant distribution, thereby minimizing guest–guest interactions and concentration quenching phenomena.

In summary, we show that using higher PDM guest and host molecules is an effective technique for reducing aggregation and enhancing the efficiency of PhOLED materials and that this can be measured using spatial statistics based analyses of HAADF-STEM and PL.

SUPPLEMENTARY MATERIAL

See the supplementary material for the photoluminescence data that were analyzed herein and additional HAADF-STEM images of each system analyzed, along with the spatial statistical analysis of each image.

ACKNOWLEDGMENTS

Theory development and analysis was supported by the U.S. Department of Energy, Office of Science, Basic Energy Sciences under Award No. DE-SC0018021. Device fabrication, TRPL measurement capabilities, and our high-performance computing node were funded by Universal Display Corporation (UDC). The HAADF-STEM portion of this research was supported by the Center for Nanophase Materials Sciences (CNMS), which is a U.S. Department of Energy, Office of Science User Facility at Oak Ridge National Laboratory.

AUTHOR DECLARATIONS

Conflict of Interest

The authors have no conflicts to disclose.

Author Contributions

Paul Niyonkuru: Conceptualization (equal); Data curation (lead); Formal analysis (equal); Investigation (equal); Methodology (equal); Writing – original draft (lead). **Roland Bennett**: Data curation (supporting); Formal analysis (equal); Investigation (supporting); Methodology (supporting); Writing – original draft (supporting). **Michael J. Zachman**: Data curation (supporting); Formal analysis (supporting); Resources (supporting); Writing – original draft (supporting). **Jeramy D. Zimmerman**: Conceptualization (equal); Formal analysis (equal); Funding acquisition (lead); Methodology (equal); Project administration (lead); Resources (lead); Supervision (lead); Writing – review & editing (lead).

DATA AVAILABILITY

The data that support the findings of this study are available from the corresponding author upon reasonable request.

REFERENCES

[1]M. A. Baldo, D. F. O'Brien, Y. You, A. Shoustikov, S. Sibley, M. E. Thompson, and S. R. Forrest, "Highly efficient phosphorescent emission from organic electroluminescent devices," Nature **395**, 151 (1998).

[2]A. C. Jacko, B. J. Powell, and R. H. McKenzie, "Sensitivity of the photophysical properties of organometallic complexes to small chemical changes," J. Chem. Phys. **133**, 124314 (2010).

[3]Y. Ma, H. Zhang, J. Shen, and C. Che, "Electroluminescence from triplet metal-ligand charge-transfer excited state of transition metal complexes," Synth. Met. **94**, 245–248 (1998).

[4]H. Yersin and W. J. Finkenzeller, *Triplet Emitters for Organic Light-Emitting Diodes: Basic Properties* (■, 2008), ISBN: 9783527405947.

[5]A. J. Browne, A. Krajewska, and A. S. Gibbs, "Quantum materials with strong spin-orbit coupling: Challenges and opportunities for materials chemists," J. Mater. Chem. C **9**, 11640–11654 (2021).

[6]B. J. Powell, "Conservation laws, radiative decay rates, and excited state localization in organometallic complexes with strong spin-orbit coupling," Sci. Rep. **5**, 10815 (2015).

[7]S. Reineke, G. Schwartz, K. Walzer, M. Falke, and K. Leo, "Highly phosphorescent organic mixed films: The effect of aggregation on triplet-triplet annihilation," Appl. Phys. Lett. **94**, 163305 (2009).

[8]Y. Kawamura, K. Goushi, J. Brooks, J. J. Brown, H. Sasabe, and C. Adachi, "100% phosphorescence quantum efficiency of Ir(III) complexes in organic semiconductor films," Appl. Phys. Lett. **86**, 071104 (2005).

[9]Y. Kawamura, J. Brooks, J. J. Brown, H. Sasabe, and C. Adachi, "Intermolecular interaction and a concentration-quenching mechanism of phosphorescent Ir(III) complexes in a solid film," Phys. Rev. Lett. **96**, 017404 (2006).

[10]C. W. Brian and L. Yu, "Surface self-diffusion of organic glasses," J. Phys. Chem. A **117**, 13303 (2013).

[11]C. R. Daley, Z. Fakhraai, M. D. Ediger, and J. A. Forrest, "Comparing surface and bulk flow of a molecular glass former," Soft Matter **8**, 2206–2212 (2012).

[12]Y. Zhang and Z. Fakhraai, "Decoupling of surface diffusion and relaxation dynamics of molecular glasses," Proc. Natl. Acad. Sci. U. S. A. **114**, 4915–4919 (2017).

[13]K. Bagchi and M. D. Ediger, "Controlling structure and properties of vapor-deposited glasses of organic semiconductors: Recent advances and challenges," J. Phys. Chem. Lett. **11**, 6935–6945 (2020).

[14]M. D. Ediger, J. De Pablo, and L. Yu, "Anisotropic vapor-deposited glasses: Hybrid organic solids," Acc. Chem. Res. **52**, 407–414 (2019).

[15]M. B. Jaskot, "Linking morphology to electronic properties in small-molecular organic semiconductors," ■ ■, ■ (■).

[16]F. Tenopala-Carmona, O. S. Lee, E. Crovini, A. M. Neferu, C. Murawski, Y. Olivier, E. Zysman-Colman, and M. C. Gather, "Identification of the key parameters for horizontal transition dipole orientation in fluorescent and TADF organic light-emitting diodes," Adv. Mater. **33**, 2100677 (2021).

[17]K. L. Kearns, S. F. Swallen, M. D. Ediger, T. Wu, and L. Yu, "Influence of substrate temperature on the stability of glasses prepared by vapor deposition," J. Chem. Phys. **127**, 154702 (2007).

[18]Y. Z. Chua, M. Ahrenberg, M. Tylinski, M. D. Ediger, and C. Schick, "How much time is needed to form a kinetically stable glass? AC calorimetric study of vapor-deposited glasses of ethylcyclohexane," J. Chem. Phys. **142**, 054506 (2015).

[19]K. L. Kearns, P. Krzyskowski, and Z. Devereaux, "Using deposition rate to increase the thermal and kinetic stability of vapor-deposited hole transport layer glasses via a simple sublimation apparatus," J. Chem. Phys. **146**, 203328 (2017).

[20]C. Bishop, Y. Li, M. F. Toney, L. Yu, and M. D. Ediger, "Molecular orientation for vapor-deposited organic glasses follows rate-temperature superposition: The case of posaconazole," J. Phys. Chem. B **124**, 2505–2513 (2020).

[21]Y. Chen, Z. Chen, M. Tylinski, M. D. Ediger, and L. Yu, "Effect of molecular size and hydrogen bonding on three surface-facilitated processes in molecular glasses: Surface diffusion, surface crystal growth, and formation of stable glasses by vapor deposition," J. Chem. Phys. **150**, 024502 (2019).

[22]A. Laventure, A. Gujral, O. Lebel, C. Pellerin, and M. D. Ediger, "Influence of hydrogen bonding on the kinetic stability of vapor-deposited glasses of triazine derivatives," J. Phys. Chem. B **121**, 2350–2358 (2017).

[23]Y. Chen, M. Zhu, A. Laventure, O. Lebel, M. D. Ediger, and L. Yu, "Influence of hydrogen bonding on the surface diffusion of molecular glasses: Comparison of three triazines," J. Phys. Chem. B **121**, 7221–7227 (2017).

[24]Y. H. Kim, T. H. Han, C. Lee, Y. H. Kim, Y. Yang, and T. W. Lee, "Molecular-scale strategies to achieve high efficiency and low efficiency roll-off in simplified solution-processed organic light-emitting diodes," Adv. Funct. Mater. **30**, 2005292 (2020).

[25]R. Ranecki, B. Baumann, S. Lach, and C. Ziegler, "Self-assembly of the chiral donor–acceptor molecule DCzDCN on Cu(100)," ACS Appl. Mater. Interfaces **16**, 9108 (2024).

[26]Y. J. Cho, K. S. Yook, and J. Y. Lee, "A universal host material for high external quantum efficiency close to 25% and long lifetime in green fluorescent and phosphorescent OLEDs," Adv. Mater. **26**, 4050–4055 (2014).

[27]T. Tsuboi and N. Aljaroudi, "Energy transfer between Ir(ppy)$_3$ molecules in neat film and concentration quenching of phosphorescence," Opt. Mater. **30**, 1375–1381 (2008).

[28]J. Kalinowski, W. Stampor, M. Cocchi, D. Virgili, V. Fattori, and P. Di Marco, "Triplet energy exchange between fluorescent and phosphorescent organic molecules in a solid state matrix," Chem. Phys. **297**, 39–48 (2004).

[29]E. B. Namdas, A. Ruseckas, I. D. Samuel, S. C. Lo, and P. L. Burn, "Photophysics of *fac*-tris(2-phenylpyridine) iridium(III) cored electroluminescent dendrimers in solution and films," J. Phys. Chem. B **108**, 1570–1577 (2004).

[30]S. Reineke, T. C. Rosenow, B. Lüssem, and K. Leo, "Improved high-brightness efficiency of phosphorescent organic LEDs comprising emitter molecules with small permanent dipole moments," Adv. Mater. **22**, 3189–3193 (2010).

[31]Y. Li, W. Shan, M. J. Zachman, M. Wang, S. Hwang, H. Tabassum, J. Yang, X. Yang, S. Karakalos, Z. Feng, G. Wang, and G. Wu, "Atomically dispersed dual-metal site catalysts for enhanced CO_2 reduction: Mechanistic insight into active site structures," Angew. Chem., Int. Ed. **61**, e202205632 (2022).

[32]A. Ligthart, X. de Vries, L. Zhang, M. C. Pols, P. A. Bobbert, H. van Eersel, and R. Coehoorn, "Effect of triplet confinement on triplet–triplet annihilation in organic phosphorescent host–guest systems," Adv. Funct. Mater. **28**, 1804618 (2018).

[33]B. D'Andrade and S. R. Forrest, "Formation of triplet excimers and dimers in amorphous organic thin films and light emitting devices," Chem. Phys. **286**, 321–335 (2003).

[34]S. Takayasu, T. Suzuki, and K. Shinozaki, "Intermolecular interactions and aggregation of *fac*-tris(2-phenylpyridinato-C^2,N)iridium(III) in nonpolar solvents," J. Phys. Chem. B **117**, 9449–9456 (2013).

[35]L. Murphy, P. Brulatti, V. Fattori, M. Cocchi, and J. A. Williams, "Blue-shifting the monomer and excimer phosphorescence of tridentate cyclometallated platinum(II) complexes for optimal white-light OLEDs," Chem. Commun. **48**, 5817–5819 (2012).

[36]T. Kobayashi, N. Ide, N. Matsusue, and H. Naito, "Temperature dependence of photoluminescence lifetime and quantum efficiency in neat *fac*-Ir(ppy)$_3$ thin films," Jpn. J. Appl. Phys. **44**, 1966–1969 (2005).

[37]T. Hofbeck and H. Yersin, "The triplet state of *fac*-Ir(ppy)$_3$," Inorg. Chem. **49**, 9290–9299 (2010).

[38]A. Köhler and H. Bässler, "Triplet states in organic semiconductors," Mater. Sci. Eng. R: Rep. **66**, 71–109 (2009).

[39]A. F. Rausch, M. E. Thompson, and H. Yersin, "Matrix effects on the triplet state of the OLED emitter Ir(4,6-dFppy)$_2$(pic) (FIrpic): Investigations by high-resolution optical spectroscopy," Inorg. Chem. **48**, 1928–1937 (2009).

[40]K. Goushi, Y. Kawamura, H. Sasabe, and C. Adachi, "Unusual phosphorescence characteristics of Ir(ppy)$_3$ in a solid matrix at low temperatures," Jpn. J. Appl. Phys. **43**, L937 (2004).

[41]A. Baddeley, E. Rubak, and R. Turner, *Spatial Point Patterns: Methodology and Applications with R*, *Chapman & Hall/CRC Interdisciplinary Statistics* (CRC Press, 2015), ISBN: 9781482210217, https://books.google.com/books?id=rGbmCgAAQBAJ.

[42]A. Proudian (2023). "RAPT: R for atom probe tomography," GitHub. https://github.com/aproudian2/rapt
[43]G. B. Vincent, A. P. Proudian, and J. D. Zimmerman, "Three dimensional cluster analysis for atom probe tomography using Ripley's K-function and machine learning," Ultramicroscopy **220**, 113151 (2021).
[44]R. A. Bennett, A. P. Proudian, and J. D. Zimmerman, "Cluster characterization in atom probe tomography: Machine learning using multiple summary functions," Ultramicroscopy **247**, 113687 (2023).
[45]R. Bennett, P. Niyonkuru, M. J. Zachman, and J. D. Zimmerman, personal communication (■ ■ ■).
[46]M. A. Kiskowski, J. F. Hancock, and A. K. Kenworthy, "On the use of Ripley's K-function and its derivatives to analyze domain size," Biophys. J. **97**, 1095–1103 (2009).
[47]P. Peumans, S. Uchida, and S. R. Forrest, "Efficient bulk heterojunction photovoltaic cells using small molecular-weight organic thin films," in *Materials for Sustainable Energy: A Collection of Peer-Reviewed Research and Review Articles from Nature Publishing Group* (■, 2010), Vol. 425, pp. 94–98.
[48]K. Kawasaki, "Anomalous spin diffusion in ferromagnetic spin systems," J. Phys. Chem. Solids **28**, 1277–1283 (1967).
[49]P. K. Watkins, A. B. Walker, and G. L. Verschoor, "Dynamical Monte Carlo modelling of organic solar cells: The dependence of internal quantum efficiency on morphology," Nano Lett. **5**, 1814–1818 (2005).
[50]M. C. Heiber and A. Dhinojwala, "Efficient generation of model bulk heterojunction morphologies for organic photovoltaic device modeling," Phys. Rev. Appl. **2**, 014008 (2014).
[51]A. R. Moore, G. Huang, S. Wolf, P. J. Walsh, Z. Fakhraai, and R. A. Riggleman, "Effects of microstructure formation on the stability of vapor-deposited glasses," Proc. Natl. Acad. Sci. U. S. A. **116**, 5937–5942 (2019).
[52]M. Shibata, Y. Sakai, and D. Yokoyama, "Advantages and disadvantages of vacuum-deposited and spin-coated amorphous organic semiconductor films for organic light-emitting diodes," J. Mater. Chem. C **3**, 11178–11191 (2015).
[53]Y. Chen, W. Zhang, and L. Yu, "Hydrogen bonding slows down surface diffusion of molecular glasses," J. Phys. Chem. B **120**, 8007–8015 (2016).
[54]S. Ruan, W. Zhang, Y. Sun, M. D. Ediger, and L. Yu, "Surface diffusion and surface crystal growth of *tris*-naphthyl benzene glasses," J. Chem. Phys. **145**, 064503 (2016).